RSC Advances



PAPER

View Article Online
View Journal | View Issue



Cite this: *RSC Adv.*, 2025, **15**, 19610

# Robust and stable $TiO_2/Al_2O_3–SiO_2$ membrane with enhanced flux and antifouling performance for organic dye removal†

Qi Deng, [a] Jing Yang*[a] and Yuzhi Ai[b]

$Al_2O_3–SiO_2$ membranes were modified with a titanium source, tetrabutyl orthotitanate (TBOT), using the sol–gel method to prepare $TiO_2/Al_2O_3–SiO_2$ composite membranes, whose performance was tested with various ionic dyes. The membrane with $n_{Ti}$ = 0.15 exhibited the best filtration performance, considering the rejection and membrane flux. Membrane flux was over 15% higher than that of the original membrane, whereas rejection decreased by only 2%. The experimental data were analyzed to estimate the solute transport parameter and the mass transfer coefficient ($k$) using the Combined Film Theory-Solution-Diffusion (CFSD) membrane transport model. The adsorption of $Al_2O_3–SiO_2$ and $TiO_2/Al_2O_3–SiO_2$ membranes was investigated using the D–R isotherm model. It was found that cationic dyes adsorbed well on both membranes, and the adsorption binding force of the original membrane for dyes was strong, which is the reason for its poor antifouling performance. The anionic dye RB-KNB was less likely to cause membrane fouling. After six cycles of filtering the RB-KNB solution, the FRR increased from 79.9% for the original membrane to 93.8% for the modified membrane, further demonstrating that the antifouling performance of the membrane had been highly enhanced. Clearly, the obtained $TiO_2/Al_2O_3–SiO_2$ membrane possesses high application potential for textile wastewater treatment.

Received 14th April 2025
Accepted 25th May 2025

DOI: 10.1039/d5ra02616d

rsc.li/rsc-advances



## 1. Introduction

Dyes are used in large quantities across a wide range of industries and water pollution caused by untreated wastewater discharged from various industries are a major environmental concern.[1] Globally, nearly 700 000 tons of dyes are consumed in various sectors, of which about 10–15% is disposed of in wastewater.[2] Among the types of dyes, anionic dyes account for the largest share, ranging from 32% to 90% in wastewater.[3] Although dye usage is inevitable, it greatly increases the risk of water contamination, resulting in a serious issue. The long-term benefits to human development could be profound if efficient and convenient methods are implemented to recycle water resources from dye wastewater, which is characterized by high chromaticity, significant organic content, considerable fluctuations in water quality, substantial discharge rates, and challenging treatment requirements.[4]

Numerous advanced technologies have been developed to treat dyeing effluents of varying chemical compositions. These methods can be broadly categorized into three groups: physical, chemical, and biological. Commonly used treatment technologies include flocculation/coagulation, precipitation, adsorption, membrane filtration, biological oxidation, ion exchange, and photocatalytic degradation, which vary in terms of efficiency, cost, and environmental impact. Membrane filtration can remove more contaminants than any other treatment method by preventing the passage of contaminants through physical barriers, chemical adsorption, or a combination of both. The benefits of membrane separation technology include excellent filtering purity during the separation process, minimal energy consumption, and environmental sustainability.

Compared to organic membranes, inorganic membranes have greater chemical and thermal stability, stronger resistance to fouling, higher separation efficiency, and enhanced membrane regeneration capability. Inorganic membranes are classified as carbon, zeolite, silica, ceramic, liquid, dynamic, and inorganic–organic hybrid membranes.[5] $SiO_2$ and $Al_2O_3$ monolayer ceramic membranes have been thoroughly investigated for removing dyeing solutions. Thu *et al.*[6] used rice husk as a raw material to prepare mesoporous $SiO_2$ for the removal of methylene blue (MB) from aqueous solutions. After 50 minutes of adsorption, the MB removal rate increased to 91.9%. The ideal dosage of $SiO_2$ for this task was 0.05 g. In a study by Soma *et al.*,[7] $Al_2O_3$ microfiltration membranes with a mean pore size of 0.2 μm were used to treat wastewater from the printing and dyeing industries. It was found that the addition of surfactants could increase the removal of soluble dyes by more than 97%; in

[a]School of Urban Planning and Municipal Engineering, Xi'an Polytechnic University, Xi'an 710048, China. E-mail: jingy76@163.com

[b]Shaanxi Department of Industry and Information Technology Comprehensive Guarantee Center, Xi'an 710054, China

† Electronic supplementary information (ESI) available. See DOI: https://doi.org/10.1039/d5ra02616d

a pilot test using ceramic membranes, dye removal was 80%, chemical oxygen demand (COD) removal was 40%, and membrane flux was 260–280 L $m^{-2}$ $h^{-1}$.

Anatase $TiO_2$ has demonstrated promising application prospects in wastewater treatment and bactericidal self-cleaning due to its strong photocatalytic performance, large specific surface area, strong oxidizing ability and lack of secondary pollution.[8] Incorporating anatase $TiO_2$ improves the antifouling performance of $Al_2O_3$–$SiO_2$ membranes. Additionally, the addition of $TiO_2$ may alter the phase composition, microstructure, and surface morphology of the composite material, significantly affecting the membrane's separation ability.[9] The literature[10–12] reveals that the majority of research on composite membranes has been centered on aspects such as preparation methods, phase structures, pore structures, micromorphologies, and gas separation applications. However, there has been limited investigation concerning the treatment of dye solutions. Thus, the sol–gel method was used in this work to prepare the ultrafiltration $Al_2O_3$–$SiO_2$ composite membrane, and the doping of $TiO_2$ modified the $Al_2O_3$–$SiO_2$ composite membrane. Initial investigations were conducted to ascertain the filtration operating conditions of $Al_2O_3$–$SiO_2$ and $TiO_2$/$Al_2O_3$–$SiO_2$ composite membranes. The applicability of the composite membranes to the filtration of dyes with varying molecular weights and ionic types was then explored. A theoretical foundation for the industrial preparation of ultrafiltration $Al_2O_3$–$SiO_2$ and $TiO_2$/$Al_2O_3$–$SiO_2$ composite membranes was established using the experimental data, which made it possible to determine the filtration mechanism of ceramic composite membranes on various dyes. Additionally, the information offered a workable operational foundation for their use in the treatment of dye wastewater and other industrial domains.

## 2. Experimental

### 2.1. Chemicals

In our experiments, the raw materials included tetraethyl orthosilicate (TEOS, AR, Chengdu Kelong Chemical Reagent Factory, Chengdu, China), absolute ethanol (EtOH, AR, Tianjin Fuyu Fine Chemical Co., Ltd, Tianjin, China), nitric acid ($HNO_3$, AR, Sichuan Xilong Chemical Co., Ltd, Sichuan, China), aluminium isopropoxide (AIP, AR, Chengdu Kelong Chemical Reagent Factory, Chengdu, China), *N*,*N*-dimethylformamide (DMF, AR, Tianjin Kemiou Chemical Reagent Co., Ltd, Tianjin, China), tetrabutyl orthotitanate (TBOT, AR, Tianjin Kemiou Chemical Reagent Co., Ltd, Tianjin, China).

### 2.2. Fabrication of sols

**2.2.1. Fabrication of $SiO_2$ sols.** The samples were prepared by the sol–gel method with TEOS as the silicon source, EtOH as the solvent, and $HNO_3$ as the catalyst. The molar ratio of TEOS/EtOH/$H_2O$/$HNO_3$ was controlled at 1/3.8/5/0.085. TEOS and EtOH were mixed to form a homogeneous solution and stirred for 40 min at room temperature. Subsequently, $H_2O$ and $HNO_3$ were added dropwise to the homogenous solution of TEOS and EtOH. After rapidly stirring the mixture and refluxing it for 3 h at 60 °C, the translucent and colorless $SiO_2$ sol was obtained.

**2.2.2. Fabrication of $Al_2O_3$ sols.** AIP was used as the aluminum source and $HNO_3$ as the catalyst. The molar ratio of AIP/$H_2O$/$HNO_3$ was controlled to be 1/100/0.25. Three flasks containing deionized water were heated to 80 °C. AIP, which was ground into powder in advance, was slowly added to deionized water, fully hydrolyzed for 1.5 h, and then $HNO_3$ was gradually added. At 85 °C, the mixture was aggressively stirred, refluxed for 8 h, and then cooled to obtain a pale blue $Al_2O_3$ sol.

**2.2.3. Fabrication of $TiO_2$ sols.** The molar ratio of TBOT/EtOH/$H_2O$/$HNO_3$ was 1/50/4/0.2. TBOT was first added to EtOH and thoroughly dissolved by stirring it for 30 min at 30 °C. Then, the mixture of $H_2O$ and $HNO_3$ was added dropwise to the homogeneous solution of TBOT and EtOH, stirred vigorously for 2 h, and cooled naturally to obtain a light yellow transparent $TiO_2$ sol.

**2.2.4. Fabrication of $TiO_2$/$Al_2O_3$–$SiO_2$ sols.** According to the Al/TEOS molar ratio ($n_{Al}$) of 0.3, the obtained $Al_2O_3$ sol was added dropwise to the $SiO_2$ sol diluted with absolute ethanol in this work and mixed thoroughly at room temperature for 40 min. Next, in accordance with different Ti/TEOS molar ratios, the prepared $TiO_2$ sol was added dropwise to the $Al_2O_3$–$SiO_2$ sol. The $TiO_2$/$Al_2O_3$–$SiO_2$ composite sol was obtained by fully mixing for 40 min at room temperature. The molar ratios of Ti/TEOS ($n_{Ti}$) are 0, 0.03, 0.08, 0.1 and 0.3, respectively.

### 2.3. Fabrication of unsupported $TiO_2$/$Al_2O_3$–$SiO_2$ materials

The prepared $TiO_2$/$Al_2O_3$–$SiO_2$ composite sol was dried in a vacuum drying oven at 40 °C and then ground into a fine powder with an onyx mortar to obtain the $TiO_2$/$Al_2O_3$–$SiO_2$ gel material. Finally, the gel material was heated to 350 °C at a heating rate of 0.5 °C $min^{-1}$ in a tube furnace, kept for 2 h, and then cooled naturally to obtain the $TiO_2$/$Al_2O_3$–$SiO_2$ unsupported body membrane material.

### 2.4. Fabrication of $TiO_2$/$Al_2O_3$–$SiO_2$ membranes

The pretreated $\alpha$-$Al_2O_3$ composite disc support was immersed in the $TiO_2$/$Al_2O_3$–$SiO_2$ sol diluted with 3 times ethanol for 6 s and withdrawn at a rate of 10 cm $min^{-1}$. After dip coating, the membrane support was placed in a drying oven with a vacuum degree of −0.08 MPa and a temperature of 30 °C for 2 h and then placed in a tube furnace for roasting. The calcination process was the same as that of the unsupported membrane material, and calcining temperature was increased to 350 °C at a rate of 0.5 °C $min^{-1}$ and maintained for 2 h. The four-time repetitions, with natural cooling, can be done to minimize the defects caused by dust in the air; thus, the $TiO_2$/$Al_2O_3$–$SiO_2$ composite membrane can be obtained. The preparation process of the $TiO_2$/$Al_2O_3$–$SiO_2$ membrane material is shown in Fig. 1.

### 2.5. Characterization

Fourier transform infrared spectroscopy (FTIR) was used to analyze the functional groups of the membrane materials before and after modification by the KBr pressing method. The spectral measurements were conducted over a wavelength range

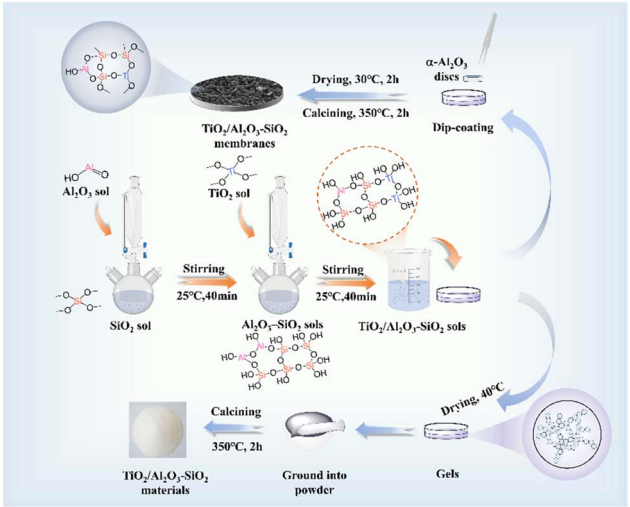


Fig. 1 Schematic of the preparation process for $TiO_2/Al_2O_3$–$SiO_2$ sols/materials/membranes.

of 400 to 4000 $cm^{-1}$. X-ray diffraction (XRD) analysis was conducted on a Rigaku D/max 2200 diffractometer, employing CuKα radiation (40 kV, 40 mA) to ascertain the chemical compositions of the materials, with a scanning range of 5° to 85° at a rate of 5° per minute. $N_2$ adsorption–desorption tests were performed on the membrane materials before and after modification using a specific surface area and pore size analyzer. $N_2$ was used as the adsorbate, dehydrated at 90 °C for 1.5 h, degassed at 250 °C for 6 h, and then tested in an instrument with a liquid nitrogen temperature of 77 K. The surface morphologies of the membranes were examined using a scanning electron microscopy (SEM, JEOL JSM-6300, Hitachi, Tokyo, Japan) operated at an accelerating voltage of 5 kV, with secondary electron signals acquired through an Everhart–Thornley detector. The contact angle tests were carried out using a contact angle goniometer (CA, JY-82, China). A laser particle size analyzer was used to evaluate the zeta potential of sols at 25 °C, and the average value was calculated after three measurements. BSD-500 platinum–cobalt colorimeter was used to detect the chroma before and after dye filtration.

### 2.6. Adsorption properties

Four dyes were selected to test the adsorption performance of the $TiO_2/Al_2O_3$–$SiO_2$ membrane: cationic dye neutral red (NR, AR, relative molecular weight ($M_w$) = 288.78, $\lambda_{max}$ = 533 nm) and methylene blue (MB, AR, relative molecular weight ($M_w$) = 373.90, $\lambda_{max}$ = 664 nm), anionic dye reactive black KNB (RB-KNB, AR, Relative molecular weight ($M_w$) = 991.82, $\lambda_{max}$ = 206 nm) and non-ionic dye disperse navy blue HGL (DNB-HGL, BS, relative molecular weight ($M_w$) = 799.80, $\lambda_{max}$ = 225 nm). NR, MB and RB-KNB were purchased from Tianjin Kemiou Chemical Reagents Co., Ltd and DNB-HGL was purchased from Zhejiang Boao New Materials Co., Ltd.

The adsorbent and dye solution were poured into a conical flask, and the adsorption process was carried out at a constant temperature in a water bath shaker. After centrifuging the supernatant at a low speed, an ultraviolet-visible spectrophotometer was used to measure its absorbance. The linear equation of dye labelling was used to calculate the concentration after adsorption, and then the adsorption capacity ($q_e$) and adsorption rate were calculated according to eqn (1):

$$q_e = \frac{(C_0 - C_e) \times V}{W} \quad (1)$$

where $C_0$ and $C_e$ (mg $L^{-1}$) are the initial and equilibrium concentrations of the dye, respectively. $W$ (g) is the dry mass of the xerogels. $V$ (L) is the volume of the solution.

### 2.7. Filtration properties

The filtration performance of the membrane was evaluated at 25 °C using a cross-flow separation system. The filtration performance of the $TiO_2/Al_2O_3$–$SiO_2$ composite membrane was investigated with respect to the effects of the coating layer number, $n_{Ti}$ value, pressure and dye molecular weight. Additionally, the filtration mechanisms of $TiO_2/Al_2O_3$–$SiO_2$ composite membranes for the four dyes were further investigated.

The membrane flux and rejection rate of an inorganic membrane reflect its filtration and separation performance, while the flux indicates the fluid transmission rate. The membrane flux represents the total amount of liquid after passing through a certain membrane area at a certain time. The calculation eqn (2):

$$J = \frac{V}{A \times T} \quad (2)$$

Here, $J$ (L $m^2$ $h^{-1}$) represents membrane flux. $A$ ($m^2$) is the effective area of the membrane. $T$ (h) is the transit time. $V$ (L) is the liquid volume.

The rejection rate reflects the separation effect of the fluid after passing through the membrane. The effect of membrane interception is often quantified in percentage form by measuring the ratio of the solute concentration in the solution before and after membrane filtering. Eqn (3) is as follows:

$$R = \left(1 - \frac{C_1}{C_2}\right) \times 100\% \quad (3)$$

where $R$ (%) represents the retention rate. $C_1$ (mol $L^{-1}$) represents the concentration of the permeate component. $C_2$ (mol $L^{-1}$) represents the feed component concentration.

### 2.8. Estimation of membrane transport parameters using the CFSD model

The membrane theory is widely used to estimate the solute transport parameter $D_{AM} \times K/\delta$ and mass transfer coefficient $k$ in the membrane. The Combined Film Theory-Solution-Diffusion (CFSD) model combines the dissolution-diffusion model with the along-membrane theory.[13] The current working equation for the CFSD model is given as eqn (4).[14] $D_{AM} \times K/\delta$ and $k$ have important effects on the rejection and membrane flux. $D_{AM} \times K/\delta$ is an important index of membrane transport performance, which reflects the diffusion and transport capacity of the solute in the membrane. In general, the larger the parameter $D_{AM} \times K/\delta$, the easier it is for the solute to pass through the membrane,

which may lead to a decrease in the rejection rate. $k$ describes the mass transfer rate of the solute in the boundary layer of the membrane surface. The larger $k$ indicates that the mass transfer rate of the solute in the boundary layer is fast, which enables the solute to reach the membrane surface more quickly. This, in turn, facilitates the solute to pass through the membrane, which may increase the membrane flux. The relationship data between $R_o$ and $J_v$, obtained by each group under constant feed concentration, constant feed rate and different pressures, can be used to numerically estimate the values $D_{AM} \times K/\delta$ and $k$. Plotting graph $\ln((1 - R_o) \times J_v/R_o)$ *vs.* $J_v$, where $\ln(D_{AM} \times K/\delta)$ is the intercept and $1/k$ is the slope, allows one to determine $\ln(D_{AM} \times K/\delta)$ and $k$.

$$\ln\left(\frac{(1 - R_o) \times J_v}{R_o}\right) = \ln\left(\frac{D_{AM} \times K}{\delta}\right) + \frac{J_v}{k} \quad (4)$$

where $R_o$ (%) is rejection. $J_v$ (m $s^{-1}$) is the membrane flux. $K$ is the partition coefficient. $D_{AM}$ ($m^2$ $s^{-1}$) represents the diffusion coefficient of the solute in the membrane. $\delta$ (m) is the thickness of the membrane. $k$ (m $s^{-1}$) is the mass transfer coefficient. $D_{AM} \times K/\delta$ (m $s^{-1}$) is a comprehensive parameter referred to as the solute transport parameter.

Eqn (5) is obtained by differentiating eqn (4) with respect to $J_v$ and setting this derivative to zero.

$$J_{v,min} = k \quad (5)$$

Here, $J_{v,min}$ is the minimum value when $R_o$ is the maximum.

### 2.9. Dye pollution resistant evaluation

The cationic NR and anionic RB-KNB were used as organic pollutants to determine the antifouling performance of the optimal membranes. The following is the filtration process: first, after 30 min of filtering pure water, the pure water flux of freshly made membranes ($f_w$) was determined. The dye solution was then filtered for 2 h to determine the membrane filtration performance, which was represented by dye flux ($f_d$). After that, pure water recovery flux ($f_r$) was calculated by rinsing the filter membrane with pure water for 30 min. One filtration cycle was defined as filtering the dye solution for 2 h and pure water for 30 min. Flux recovery rate (FRR), total flux decline rate (TFR), reversible flux decline rate (RFR), and irreversible flux decline rate (IFR) were used to assess the antifouling performance of the membrane. These parameters are calculated using the following formulas (6)–(9):[15]

$$FRR = \frac{f_r}{f_w} \times 100\% \quad (6)$$

$$RFR = \left(\frac{f_r - f_d}{f_w}\right) \times 100\% \quad (7)$$

$$IFR = \left(\frac{f_w - f_r}{f_w}\right) \times 100\% \quad (8)$$

$$TFR = \left(1 - \frac{f_d}{f_w}\right) \times 100\% = RFR + IFR \quad (9)$$

## 3. Results and discussion

### 3.1. Phase-chemical structure analysis

The infrared spectra of unsupported $TiO_2/Al_2O_3$–$SiO_2$ materials modified by different $TiO_2$ doping contents are shown in Fig. 2(a). A peak of absorption is seen in all $TiO_2/Al_2O_3$–$SiO_2$ materials at 3450 $cm^{-1}$, which is associated with the –OH stretching vibration of the surface-adsorbed water and structural coordination water.[16] The hydroxyl groups (O–H) on the surface of $TiO_2$ are responsible for the band at 3429 $cm^{-1}$. The bending vibration peak of –OH in the physically adsorbed water is reflected by an absorption peak at 1640 $cm^{-1}$.[17] The absorption peak of the $TiO_2/Al_2O_3$–$SiO_2$ material at 1089 $cm^{-1}$ is the binding peak of Si–O–Si and Al–O bonds. The two absorption peaks are similar and overlap each other. Furthermore, in the $TiO_2/Al_2O_3$–$SiO_2$ material, the Si–O–Ti bond stretching vibration peak was observed at 950 $cm^{-1}$ in contrast to the $Al_2O_3$–$SiO_2$ material.[18] For octahedrally coordinated Al, the vibration of the Al–OH bonding can be attributed to the band in the 937–980 $cm^{-1}$ range.[19] In contrast to a straightforward physical van der Waals force, the formation of the Si–O–Ti bond suggests that the bond between $TiO_2$ and $SiO_2$ is the result of a chemical reaction process. The symmetric stretching vibration peak of the Si–O bond appears at 800 $cm^{-1}$. After combining $SiO_2$ and $Al_2O_3$ sols, the reaction between Si–OH and Al–OH groups occurs, which allows some Si and Al atoms to be substituted for one another to form Si–O–Al bonds. The peak is ascribed to around 554 $cm^{-1}$.[20] In addition, due to the dehydroxylation reaction during the curing process, a more stable oxygen bridge bond was formed, and an absorption peak of Ti–O–Al–O–Si was speculated to be in the region of 500–1000 $cm^{-1}$. The hydrothermal stability of the material is enhanced by the presence of Al–O–Si and Ti–O–Al–O–Si bonds. It can be seen from the diagram that the FTIR curve shape and the position of each absorption peak of the $TiO_2/Al_2O_3$–$SiO_2$ membrane materials with different $n_{Ti}$ are roughly similar, but the intensity of individual absorption peaks changes. With the increase of $n_{Ti}$, the stretching vibration peak of the Si–O–Ti bond at 950 $cm^{-1}$ increases, and the antisymmetric stretching vibration peak of the Si–O–Si bond at 1089 $cm^{-1}$ and the O–Si–O symmetric stretching vibration peak at 800 $cm^{-1}$ decrease. As the concentration of $n_{Ti}$ increases, there is a notable enhancement in the stretching vibration peak of the Si–O–Ti bond at 950 $cm^{-1}$. Conversely, the antisymmetric stretching vibration peak of the Si–O–Si bond at 1089 $cm^{-1}$ and the symmetric stretching vibration peak of the O–Si–O bond at 800 $cm^{-1}$ exhibit a marked decrease.

Fig. 2(b) illustrates the XRD patterns of unsupported $TiO_2/Al_2O_3$–$SiO_2$ materials with different $TiO_2$ doping contents. $TiO_2/Al_2O_3$–$SiO_2$ materials have a broad diffraction peak at about $2\theta = 23.40°$, corresponding to amorphous $SiO_2$.[21,22] Three characteristic diffraction peaks of $\gamma$-$Al_2O_3$ (JCPDS 29-0063) appeared near $2\theta = 37.60°$, 45.78°, and 66.76° for each membrane material, and the corresponding crystal plane indexes were (311), (400), and (440), respectively. When the $TiO_2$ doping content is small and $n_{Ti} = 0.03$ and 0.08, the curve shape and

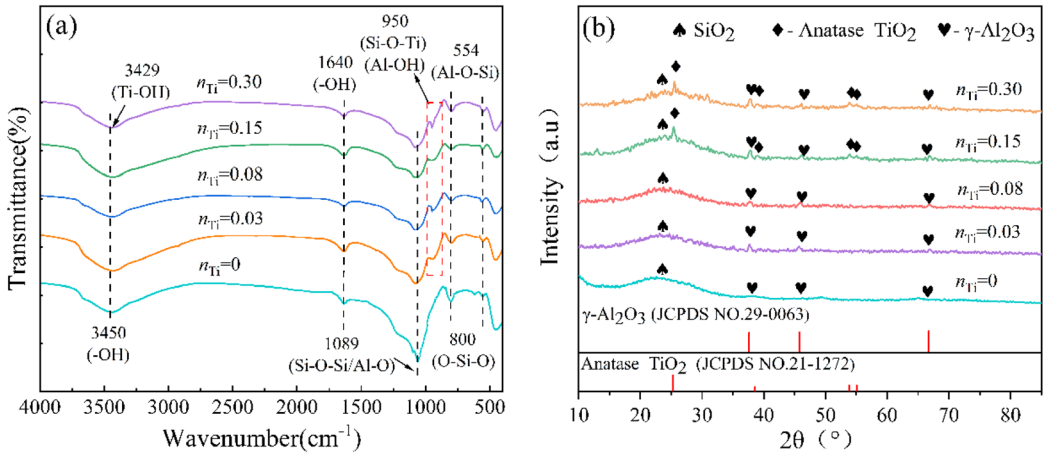


Fig. 2 (a) FTIR spectra and (b) XRD patterns of unsupported $TiO_2/Al_2O_3$–$SiO_2$ materials with different $n_{Ti}$.

position of the diffraction peaks are roughly similar due to the low $TiO_2$ doping content or due to its reaction with $SiO_2$, which could be the possible reason for no characteristic diffraction peak of anatase $TiO_2$ in the XRD spectra of the two $TiO_2/Al_2O_3$–$SiO_2$ materials. When $n_{Ti} = 0.15$ and 0.3, the characteristic diffraction peaks of anatase $TiO_2$ (JCPDS21-1272) appeared near $2\theta = 25.28°$, 38.58°, 53.89° and 55.06° in the XRD patterns of $TiO_2/Al_2O_3$–$SiO_2$ materials, and the corresponding crystal planes were (101), (112), (105) and (211), respectively. With the increase of $n_{Ti}$, the intensity of these diffraction characteristic peaks increased. It can be speculated that when $n_{Ti} \geq 0.15$, the phase structure of the $TiO_2/Al_2O_3$–$SiO_2$ material is mainly composed of amorphous $SiO_2$, γ-$Al_2O_3$ and anatase $TiO_2$.

### 3.2. Pore structure analysis

The specific surface area and pore structure of $TiO_2/Al_2O_3$–$SiO_2$ membranes with varying $n_{Ti}$ were investigated using the $N_2$ adsorption–desorption and pore size analysis processes. Their $N_2$ adsorption–desorption isotherms are shown in Fig. 3(a). It is clear that the form of the $N_2$ adsorption–desorption isotherm curves for all unsupported $TiO_2/Al_2O_3$–$SiO_2$ materials is nearly identical. At a relative pressure $P/P_0 < 0.1$, the $N_2$ adsorption capacity of the membranes rapidly increases due to the high adsorption potential energy within the pores. Consequently, the adsorption capacity of $N_2$ continues to increase gradually while the relative pressure rises. The $N_2$ adsorption–desorption isotherms of the $TiO_2/Al_2O_3$–$SiO_2$ materials exhibit hysteresis loops, which IUPAC classifies as class IV isotherms with $H_4$ hysteresis loops, suggesting that the materials are typical microporous structures. The adsorption capacity of $N_2$ rises as $n_{Ti}$ increases, improving the $N_2$ adsorption performance. The reduction in the adsorption amount of $N_2$ at $n_{Ti} = 0.3$ may be caused by pore collapse and shrinking of the internal pore structure of the $TiO_2/Al_2O_3$–$SiO_2$ material.

Fig. 3(b) shows the pore size distribution of unsupported $TiO_2/Al_2O_3$–$SiO_2$ membranes with different $n_{Ti}$. The diagram illustrates a difference in the pore size distribution of the $Al_2O_3$–$SiO_2$ material. When $n_{Ti}$ becomes larger, the maximum micropore volume of the $TiO_2/Al_2O_3$–$SiO_2$ material is mainly concentrated at 1.09–2.00 nm. It reveals that as $n_{Ti}$ increases, the pore size distribution of the $TiO_2/Al_2O_3$–$SiO_2$ material changes significantly. As the pore size distribution broadens,

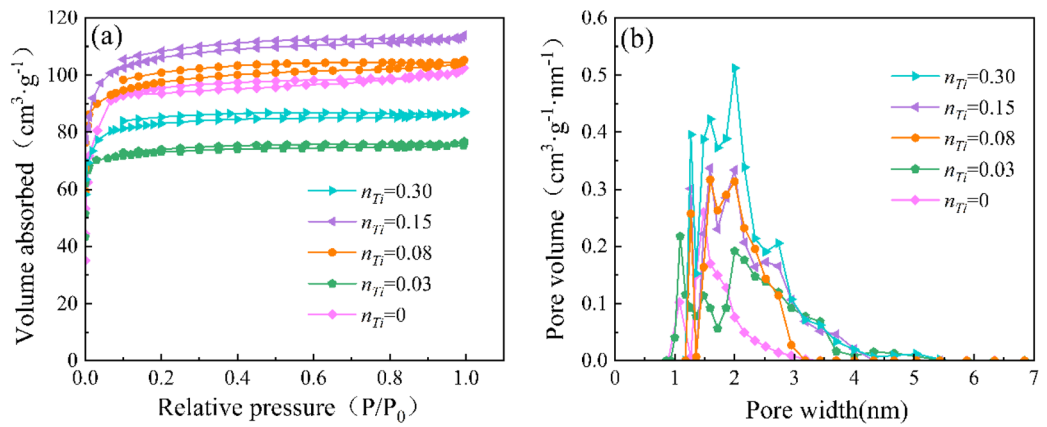


Fig. 3 (a) $N_2$ adsorption–desorption isotherms and (b) pore size distributions of unsupported $TiO_2/Al_2O_3$–$SiO_2$ membrane materials with different $n_{Ti}$.

Table 1 Pore structure parameters of $TiO_2/Al_2O_3$–$SiO_2$ membrane materials with different $n_{Ti}$

| $n_{Ti}$ | BET surface area/$m^2$ $g^{-1}$ | Micropore area/$m^2$ g | $V_T$/$cm^3$ g | $V_{Mic}$/$cm^3$ $g^{-1}$ | Mean pore width/nm |
|---|---|---|---|---|---|
| 0 | 216.427 | 102.762 | 0.130 | 0.062 | 2.348 |
| 0.03 | 181.904 | 100.796 | 0.107 | 0.037 | 2.334 |
| 0.08 | 241.771 | 143.504 | 0.149 | 0.089 | 2.405 |
| 0.15 | 278.962 | 178.240 | 0.166 | 0.110 | 2.468 |
| 0.3 | 202.853 | 110.191 | 0.113 | 0.065 | 2.555 |

the average pore size increases, the pore size distribution moves to a wider pore range, and there is a tendency from micropore distribution to mesopore distribution.

Table 1 displays the pore structure characteristics of the membranes with varying $n_{Ti}$. It can be seen that after Ti element doping, with the increase of $n_{Ti}$, the average pore size, micropore volume, total pore volume, micropore surface area and BET surface area of the $TiO_2/Al_2O_3$–$SiO_2$ membrane material increase. Because in the $TiO_2/Al_2O_3$–$SiO_2$ membrane material, part of $TiO_2$ is uniformly covered on the surface of $SiO_2$ or into the pores of $SiO_2$ with smaller particles, which will increase the micropore surface area and BET-specific surface area of the membrane material. The average pore size of the membranes, on the other hand, increases as a result of Ti atoms taking the lattice position of Si atoms and creating a new skeleton Si–O–Ti when some $TiO_2$ replaces some $SiO_2$ in the network. More anatase $TiO_2$ crystals are formed and distributed on the surface of the $SiO_2$ network when $n_{Ti} = 0.3$. The internal pore structure of the $TiO_2/Al_2O_3$–$SiO_2$ membrane material is blocked and shrinkage and pore collapse occur, resulting in a decreased total pore volume and BET-specific surface area. Therefore, combining the above analyses, it can be seen that more $TiO_2$ doping is not necessarily better; rather, the smaller the $TiO_2$ doping, the larger the microporous surface area and microporous volume percentage, the more suitable it is for filtration studies.

### 3.3. SEM analysis

Fig. 4 shows the surface electron micrographs of the membranes, respectively. The surface of the two composite materials is relatively flat, with a uniform coating, and there are no visible cracks and gaps, indicating that the coating and roasting processes are better. The $Al_2O_3$–$SiO_2$ sol was successfully dip-coated on the $\alpha$-$Al_2O_3$ support. The particle size was between 0.9 and 6.3 nm. Compared with the $Al_2O_3$–$SiO_2$ membrane, the surface particle size distribution of the $TiO_2/Al_2O_3$–$SiO_2$ composite membrane is wider, and the particle size is between 1 and 7.8 nm. Small white particles are observed on the surface of the membrane, possibly $TiO_2$ not entering the $SiO_2$ network structure and covering the surface of the membrane. The $TiO_2/Al_2O_3$–$SiO_2$ sol was successfully impregnated on the $\alpha$-$Al_2O_3$ support, with a part of the sol penetrating into the support.

### 3.4. Contact angle test

The pure water contact angle test was carried out to judge the hydrophilicity of the modified membrane. From Fig. 5, the water contact angles of $Al_2O_3$–$SiO_2$ and $TiO_2/Al_2O_3$–$SiO_2$ membranes are 63.5° and 20.1°, respectively. It can be seen that with the addition of $TiO_2$, the water contact angle decreases, indicating that the hydrophilicity of the modified membrane is enhanced, which helps water to pass through the membrane more easily during the filtration process.[23]

### 3.5. Filtration performance analysis

**3.5.1. Effect of the coating layer number.** In this experiment, the number of coating layers was used to determine membrane thickness. Fig. 6 depicts the particular impact of the number of coating layers on the RB-KNB rejection and membrane flux in the composite membrane. It is evident that for the same membrane, under similar conditions, the rejection rate of the RB-KNB solution rises and the membrane flux falls with the increase in the number of coating layers. This is because when the number of coating layers is small, holes and cracks appear on the surface or in the deeper layers of the calcined ceramic membrane, resulting in a large membrane flux

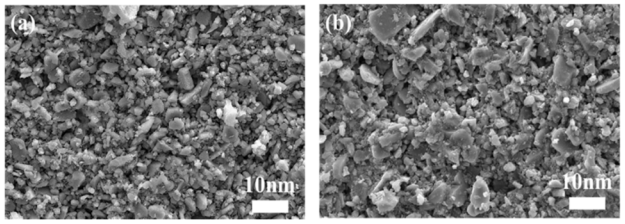


Fig. 4 SEM images of surfaces of (a) $Al_2O_3$–$SiO_2$ and (b) $TiO_2/Al_2O_3$–$SiO_2$ membranes.

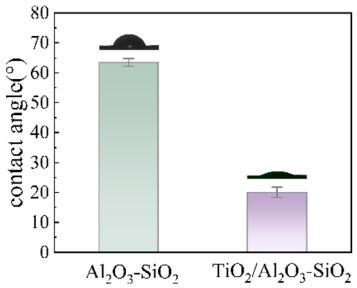


Fig. 5 Contact angle of $Al_2O_3$–$SiO_2$ and $TiO_2/Al_2O_3$–$SiO_2$ membranes.

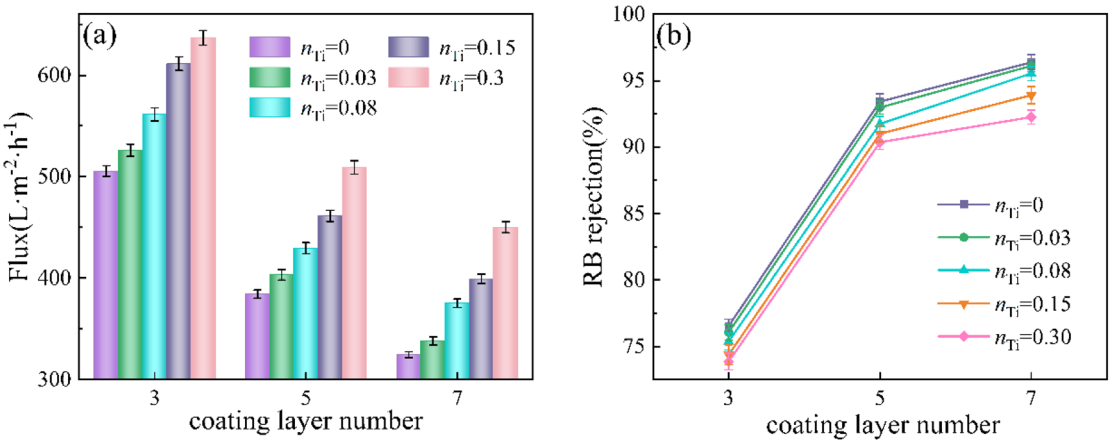


Fig. 6 (a) Membrane flux and (b) rejection of the $TiO_2/Al_2O_3$–$SiO_2$ membrane for separation of RB-KNB at different coating layers (conditions: initial dye concentration = 50 mg $L^{-1}$, contact time = 2 h, $T$ = 298 K, and pressure = 0.2 MPa).

and a low rejection rate. As the number of coating layers increases, the sol particles will repair the cracks and defects that may exist on the surface of the film. However, when the coating layer is 7, the membrane layer becomes thicker and denser, the membrane flux decreases, and the rejection rate is not significantly higher. An excellent ceramic membrane should have both a large membrane flux and a good rejection rate. Based on the evaluation of the two, the five-layer coating membrane is more in line with the experimental requirements.

**3.5.2. Effect of $n_{Ti}$.** Fig. 7 illustrates the influence of $n_{Ti}$ on flux and rejection. The membrane material exhibits a greater rejection rate for cationic dyes (NR and MB) and a higher membrane flux for anionic and nonionic dyes. The membrane flux increased rapidly as the $n_{Ti}$ increased, but the rejection of dyes by $TiO_2/Al_2O_3$–$SiO_2$ reduced gradually. Through the FTIR and $N_2$ adsorption–desorption analysis of the membranes, it can be known that a new skeleton Si–O–Ti is formed in the $TiO_2/Al_2O_3$–$SiO_2$ membrane owing to the introduction of $TiO_2$, increasing the average pore size of the membrane material.[24]

As the $n_{Ti}$ increases, the average pore size of the $TiO_2/Al_2O_3$–$SiO_2$ membrane material becomes larger, allowing dye solutions to pass through the membrane surface faster, resulting in an increased membrane flux and a reduced rejection rate. It is very important to choose an optimal $TiO_2$ doping ratio for further research. Considering the removal rate and membrane flux, $n_{Ti}$ = 0.15 is found to be more suitable.

**3.5.3. Effect of pressure difference.** Fig. 8(a) shows the effect of pressure difference at 25 °C on the filtration of RB-KNB by $Al_2O_3$–$SiO_2$ and $TiO_2/Al_2O_3$–$SiO_2$ composite membrane. Fig. 8(a) depicts the effect of a pressure variation at 25 °C on the filtration of RB-KNB by $Al_2O_3$–$SiO_2$ and $TiO_2/Al_2O_3$–$SiO_2$ composite membranes. The rejection rate of the composite membrane to RB-KNB increased first and then decreased with increasing pressure, reaching its peak at 0.2 MPa. Also, the membrane flux of the $TiO_2/Al_2O_3$–$SiO_2$ membrane is better than that of the $Al_2O_3$–$SiO_2$ membrane because as the pressure increases, concentration polarization becomes stronger and plays a leading role.

When the pressure reaches a specific level, the operational pressure plays a leading role, resulting in a progressive reduction in the rejection rate. In addition, as the pressure increases, the membrane flux gradually increases, but the increase is significantly reduced. When the external pressure is low, dye molecules begin to deposit on the membrane surface or penetrate the membrane pores, causing lighter fouling. However, as the pressure increases, more dye molecules are trapped and a boundary layer forms, reducing the increase in membrane flux.

**3.5.4. Effect of dye molecular weight.** The interception of the membrane and the adsorption and permeation of dye molecules on the membrane surface are responsible for the effect of the dye molecular weight on the performance of membrane filtration of dye wastewater. According to Fig. 8(b), the rejection rates of $TiO_2/Al_2O_3$–$SiO_2$ composite membranes for the four dyes were in the order of MB > NR > RB-KNB > DNB-HGL, with rejection rates of 93.92%, 92.61%, 91.01%, 89.98%, respectively, and the removal rates of composite membranes for the four dyes did not follow the pattern of the higher molecular weights of the dyes.

Detection of chroma before and after membrane filtration of dye wastewater is one of the commonly used methods to evaluate the treatment effect of dye wastewater. The chroma

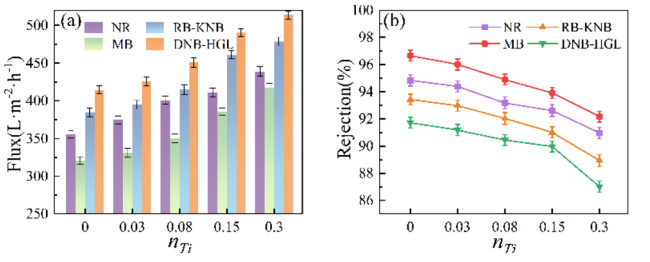


Fig. 7 Effect of $n_{Ti}$ on the (a) membrane flux and (b) rejection of the $TiO_2/Al_2O_3$–$SiO_2$ composite membrane (conditions: initial dye concentration = 50 mg $L^{-1}$, contact time = 2 h, $T$ = 298 K, and pressure = 0.2 MPa).

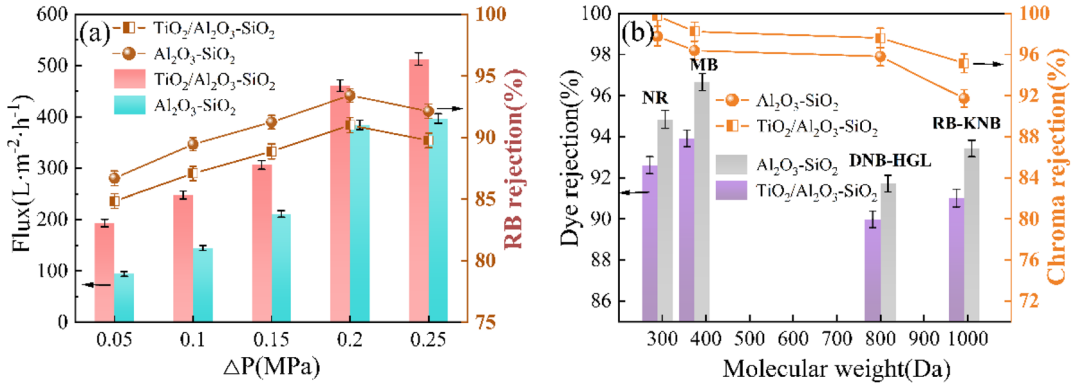


Fig. 8 Effect of (a) pressure difference and (b) dye molecular weight on the rejection rate by $Al_2O_3$–$SiO_2$ and $TiO_2/Al_2O_3$–$SiO_2$ composite membranes (conditions: initial dye concentration = 50 mg $L^{-1}$, contact time = 2 h, and $T$ = 298 K).

rejection rates of NR, MB, RB-KNB and DNB-HGL by $TiO_2/Al_2O_3$–$SiO_2$ composite membrane were 99.76%, 98.23%, 97.61% and 95.16%, respectively. In conclusion, the $TiO_2/Al_2O_3$–$SiO_2$ composite membrane has an excellent effect on color removal in dye solutions.

### 3.6. Membrane transport parameter analysis

The experimental data were analyzed using the CFSD model. Fig. 9 shows the curves of the corresponding models of RB-KNB, that is, the relationship between $\ln((1 - R_o) \times J_v/R_o)$ and $J_v$. The parameters $k$ and $D_{AM} \times K/\delta$ were determined from the plot. From Table 2, the parameters $D_{AM} \times K/\delta$ and $k$ of the $TiO_2/Al_2O_3$–$SiO_2$ membrane are larger than those of the $Al_2O_3$–$SiO_2$ membrane, indicating that the RB-KNB can migrate more quickly in the $TiO_2/Al_2O_3$–$SiO_2$ membrane, reducing the accumulation in the membrane and helping to maintain a higher flux. The model predicts the maximum rejection rate $R_{o,max}$ at the minimum flux $J_{v,min}$. The results indicate that the $TiO_2/Al_2O_3$–$SiO_2$ membrane has great potential in removing dyes from wastewater.

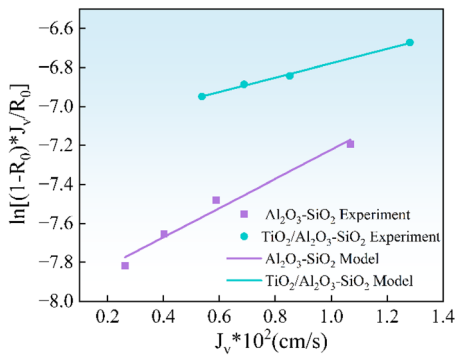


Fig. 9 CFSD model of RB-KNB onto $Al_2O_3$–$SiO_2$ and $TiO_2/Al_2O_3$–$SiO_2$ membranes.

### 3.7. Antifouling performance analysis

In this study, the D–R model was used to explore the strength of the adsorption between the membrane material and the dyes, and to estimate the adsorption energy. In the D–R model, the adsorption process is primarily driven by pore filling, with the adsorbent's porosity considered a critical factor that influences this mechanism.[25] Fig. 10(a and b) presents the nonlinear fitting results of the D–R isothermal adsorption models, while Table 3 summarizes the corresponding characteristic parameters. The calculation of the D–R model is described using eqn (10)–(12):

$$q_e = q_m e^{-K_D \varepsilon^2} \quad (10)$$

$$\varepsilon = RT \ln\left(1 + \frac{1}{C_e}\right) \quad (11)$$

$$E = \frac{1}{\sqrt{2K_D}} \quad (12)$$

Here, $q_m$ (mg $g^{-1}$) is the theoretical saturation capacity. $\varepsilon$ is the Polanyi potential. $E$ (kJ $mol^{-1}$) is the average adsorption energy. $K_D$ is the constant related to the mean free energy of adsorption.

As indicated in Table 3, the theoretical saturated adsorption capacity $q_m$ of the $Al_2O_3$–$SiO_2$ membrane for the four dyes is all larger than that of the $TiO_2/Al_2O_3$–$SiO_2$ membrane. In addition, the average adsorption energy $E$ obtained from the D–R model analysis can provide information on the adsorption mechanism and physical or chemical processes. The adsorption behavior

Table 2 Parameter estimated using the data-fitting method for RB-KNB

| Membrane | $K \times 10^2$ (cm $s^{-1}$) | $D_{AM} \times K/\delta \times 10^4$ (cm $s^{-1}$) | $J_{v,min} \times 10^2$ (cm $s^{-1}$) | $R_{o,max}$ |
|---|---|---|---|---|
| $TiO_2/Al_2O_3$–$SiO_2$ | 2.720 | 7.888 | 2.720 | 0.99 |
| $Al_2O_3$–$SiO_2$ | 1.335 | 3.453 | 1.335 | 0.99 |

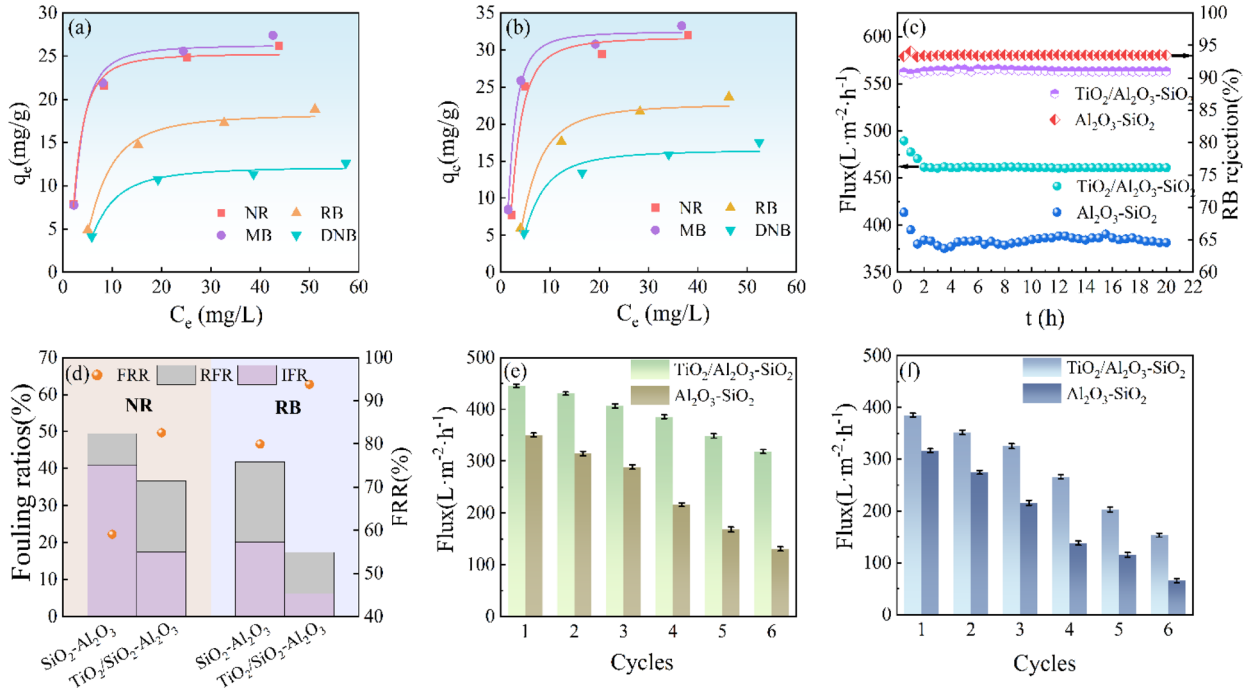


Fig. 10 D–R isotherm model of dyes onto (a) $TiO_2/Al_2O_3$–$SiO_2$ and (b) $Al_2O_3$–$SiO_2$ membranes; (c) long-time separation performance of the membrane for filtration of RB solution; (d) anti-pollution parameters of $TiO_2/Al_2O_3$–$SiO_2$ and $Al_2O_3$–$SiO_2$ membranes; and cyclic separation flux of the prepared membranes for (e) RB and (f) NR.

Table 3 D–R isotherm parameters for dye adsorption under 298 K

| Membrane | Parameters | NR | MB | RB-KNB | DNB-HGL |
|---|---|---|---|---|---|
| $TiO_2/Al_2O_3$–$SiO_2$ | $q_m$ (mg g$^{-1}$) | 25.28 | 26.29 | 18.32 | 12.17 |
| | $E$ | 5.737 | 5.722 | 2.685 | 2.643 |
| $Al_2O_3$–$SiO_2$ | $q_m$ (mg g$^{-1}$) | 31.71 | 32.49 | 22.76 | 16.51 |
| | $E$ | 6.070 | 7.661 | 3.216 | 3.044 |

was ascribed to physical and ion exchange processes when the $E$ values were within the range of 1–8 kJ mol$^{-1}$ and 8–16 kJ mol$^{-1}$, respectively, and $E$ values greater than 16 kJ mol$^{-1}$ are regarded as corresponding to chemical adsorption.[26] As presented in Table 3, the $Al_2O_3$–$SiO_2$ membrane exhibits higher $E$ values compared to the $TiO_2/Al_2O_3$–$SiO_2$ membrane. Furthermore, the $E$ values of both membranes for cationic dyes are significantly higher than those for other dye types. The higher adsorption energy implies that a more stable combination is formed between the adsorbate and the adsorbent. To some extent, the stability of the adsorption performance of the adsorbent is ensured by the fact that the adsorbate is difficult to fall off its surface when it is disturbed by external factors. However, it is easy to cause serious membrane fouling, shorten the service life of the membrane, and thus greatly increase the operating cost.

The long-term separation performance of the RB-KNB solution filtration for up to 20 h was utilized to assess the separation stability of the $TiO_2/Al_2O_3$–$SiO_2$ membrane, as shown in Fig. 10(c). After 2 h, the membrane separation property was basically stable. The permeability and rejection of the $TiO_2/Al_2O_3$–$SiO_2$ membrane remained relatively constant during the long-term separation process. Also, it has better stability than the $Al_2O_3$–$SiO_2$ membrane. This result indicates that the $TiO_2/Al_2O_3$–$SiO_2$ membrane has stable separation performance. The experimental results reveal that the $TiO_2/Al_2O_3SiO_2$ membrane has good permeability, rejection, and antifouling capabilities while filtering anionic dye solutions.

A membrane with strong antifouling performance can significantly enhance separation efficiency and minimize the number of cleaning steps, thereby significantly extending its service life.[27] This study evaluated the antifouling capabilities of the recently developed $TiO_2/Al_2O_3$–$SiO_2$ membrane by filtering the RB-KNB and NR solutions. Fig. 10(d) shows the antifouling parameters of the modified membrane and the original membrane, including FRR, RFR, and IFR. From the initial evaluation of the resistance to fouling of both membranes, it is clear that $TiO_2$ improves the overall resistance of the membrane to fouling, as evidenced by the higher FRR values than uncoated membranes. In general, the flux decline can be explained by two main aspects: the reversible fouling effect and irreversible fouling effect. Although both reversible and irreversible fouling can affect the membrane performance, the former can be 'reversed' more easily with the help of a simple hydraulic cleaning method, while the latter often requires a large number of chemical cleaning operations or direct membrane replacement. It can be seen that irreversible fouling is the main factor leading to membrane performance degradation and life reduction. The results in Fig. 10(d) indicate that the NR dye has a higher level of pollution to the $Al_2O_3$–$SiO_2$ membrane, as reflected by the larger IFR value and lower FRR value. For filtered RB-KNB and NR solutions, there was an increase in FRR from 79.9% to 93.8% and from 59.1% to

82.6%, respectively; also, the decrease in IFR was from 20.1% to 6.2% and from 40.9% to 17.4%, respectively. This could be attributed to the hydroxyl groups on the surface of the $TiO_2$ nanoparticles, which increase the hydrophilicity of the membrane surface and thus the resistance to fouling.[28,29] $TiO_2$ can improve the hydrophilicity of the membrane and reduce membrane fouling, which has been widely reported.[30] These improvements represent a significant advancement in the antifouling abilities of ceramic membranes containing $TiO_2$. In addition, the adsorption energy ($E$) calculated from the D–R curve indicates that the $TiO_2/Al_2O_3$–$SiO_2$ membrane fouling is mainly caused by physical adsorption, which makes it easier to remove anionic dyes. The $TiO_2/Al_2O_3$–$SiO_2$ membrane exhibits the lowest TFR value after filtering the RB-KNB solution, and the RFR is higher than IFR, which verifies the previous conclusion.

In general, the cycle performance test demonstrates the stability of the membrane and its ability to withstand long-term operation. Therefore, the selected membranes were subjected to 6 cycles of RB-KNB and NR filtration, with 2.5 h per cycle. Fig. 10(e) and (f) display the findings of the reusability investigation. At the end of the sixth cycle, the flux of $TiO_2/Al_2O_3$–$SiO_2$ to RB-KNB and NR solutions decreased by 30.9% and 62.6%, respectively, while the flux of $Al_2O_3$–$SiO_2$ decreased by 66.0% and 81.5%, respectively. Although the cleaning method may not completely restore the surface of the membrane, $TiO_2$ ensures better antifouling performance of the $TiO_2/Al_2O_3$–$SiO_2$ membrane, and the flux loss is lower than that of the unmodified $Al_2O_3$–$SiO_2$ membrane.

### 3.8. Filtration mechanism analysis

The filtration of NR, MB, RB-KNB and DNB-HGL by $Al_2O_3$–$SiO_2$ and $TiO_2/Al_2O_3$–$SiO_2$ composite membranes is not a simple screening mechanism. The nature of the dye, its molecular structure, and the charge interaction between the dye and the membranes all affect the different ways the membrane rejects dyes.[31]

The rejection rate of the composite membranes to the four dyes does not follow the rule that rejection rates increase with molecular weight. Fig. 11(a–d) is the molecular structure diagram of the four dyes, and Fig. 11(e) shows the surface charge properties of the two membranes under neutral pH conditions. NR dyes, on the one hand, comprise a phenazine chloride group with a cyclic molecular structure and high rejection rate. On the other hand, NR is a cationic dye that carries a positive charge in aqueous solutions due to the presence of $N^+$ ions. There are two types of interactions between composite membranes and the NR solution. One is electrostatic interactions with $N^+$ ions, and the other is adsorption caused by van der Waals forces. The composite membranes mainly intercept NR through pore size screening, physical adsorption and electrostatic interaction. The filtration mechanism of MB is similar to that of NR. The RB-KNB has more water-soluble groups and better water solubility. It is an anionic dye, and the aqueous solution is negatively charged, which is mutually exclusive with the negative charges on the two membranes, reducing the speed of dye molecules passing through the membranes and resulting in high rejection. In addition, due to the enhanced hydrophilicity and low surface roughness of the $TiO_2/Al_2O_3$–$SiO_2$ membrane, there is electrostatic repulsion between the dye and the membrane surface, which greatly reduces the amount of dye adsorbed on the membrane surface.[32] The filtration mechanism is mainly mechanical interception and adsorption interception. Studies have shown that the electrostatic repulsion between the dye molecules and the membrane surface can enhance the rejection performance of the membrane for the same charge dye, inhibit the adsorption of the dye, and improve its antifouling properties.[33] Fig. 12 shows the filtration mechanism of RB-KNB on the surface of $Al_2O_3$–$SiO_2$ and filtration $TiO_2/Al_2O_3$–$SiO_2$ membranes. DNB-HGL is an azo dye with poor water solubility. It is a non-ionic dye, and the surface charge of the composite membranes does not affect it. The N and O atoms and aromatic rings in the dye structure have hydrogen bonds with the surface of the

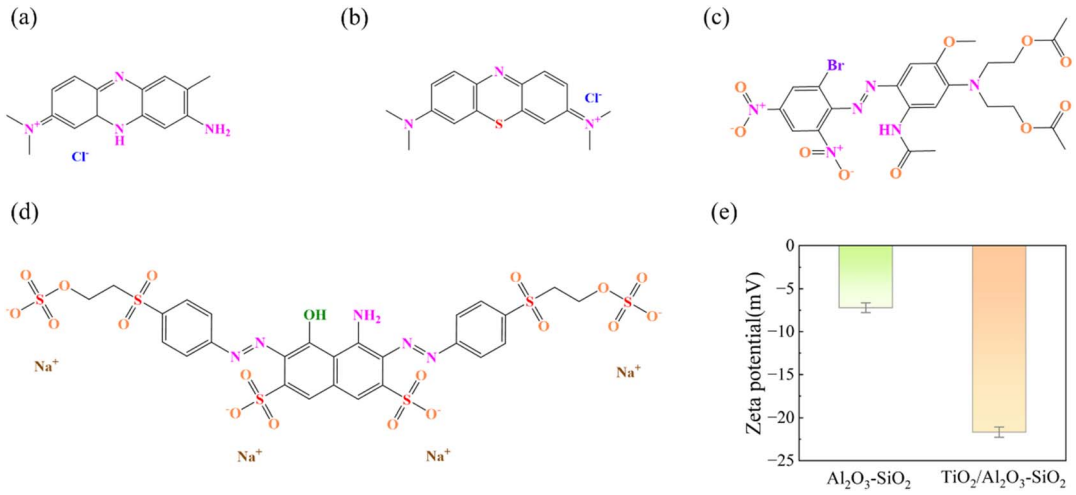


Fig. 11 Molecular structures of (a) NR, (b) MB, (c) DNB-HGL, and (d) RB-KNB and (e) zeta potential of $Al_2O_3$–$SiO_2$ and $TiO_2/Al_2O_3$–$SiO_2$ membranes.

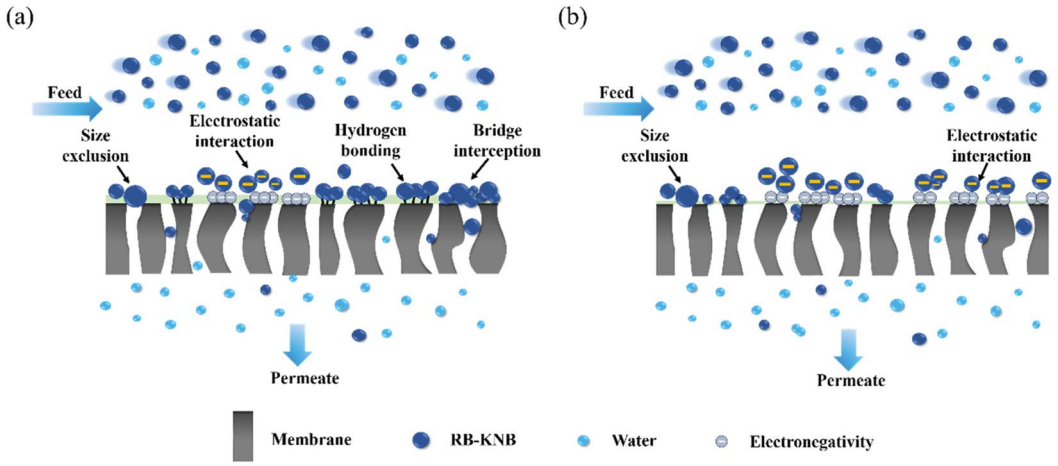


Fig. 12 Filtration mechanism of RB-KNB on the surface of (a) $Al_2O_3$–$SiO_2$ and (b) $TiO_2$/$Al_2O_3$–$SiO_2$ composite membranes.

Table 4 Literature review on modified membranes for separation of dyes

| Membrane | Flux (L $m^{-2}$ $h^1$) | Dye rejection (%) | FRR | Testing condition | Ref. |
|---|---|---|---|---|---|
| PVDF/CD-0.75/25 | 75.2 | CR (99%) | 97.6% (BSA, after 5 cycles) | 4 bar | 35 |
| PPSU/P($D_2$-$AE_1$) | 222 | CR (99.9%) | 96.2% (BSA) | 1 bar | 36 |
| Zeolite-A/polystyrene | 93.51 | DR 80 (99%) | 94.6% (DR 80) | 3 bar | 37 |
| $TiO_2$@ZIF-67/PVDF | 261.4 | RB (97.4%) | 56.2% (BSA) | 2 bar | 38 |
| PANI–$TiO_2$/PVDF | 88 | RB (81.5%) | 95% (BSA) | 2 bar | 39 |
| Ag@chitosan/PPSU | 227.48 | RB (89.27%) | 86.13% (BSA) | 2 bar | 40 |
| $Fe_3O_4$@$SiO_2$@PrEDAS | 358.6 | RB (97%)<br>RR 120 (99%) | >70% (BSA) | 2 bar | 41 |
| PES–MF | 82.7 | RB (99.76%) | 67.72% (RB) | 4 bar | 42 |
| Sepro NF 2A | 19.5 | NR (88.7%) | — | 2 bar | 43 |
| CA/GO–$TiO_2$ membrane | 31.8 | MB (99.3%) | 76.01% (BSA) | 0.9 bar | 44 |
| PS/$SiO_2$ membrane | 9.1 | MB (90.1%) | — | 4 bar | 45 |
| $TiO_2$/$Al_2O_3$–$SiO_2$ membrane | 461.3 | RB (91.0) | 88.72% (RB, after 6 cycles) | 2 bar | This study |
| | 490.2 | DB (89.9) | — | | |
| | 411.1 | NR (92.6%) | 74.32% (NR, after 6 cycles) | | |
| | 385.6 | MB (93.9%) | — | | |

material. Therefore, the filtration mechanism is mainly based on mechanical interception and adsorption interception, and the interception rate is low. The average adsorption energy ($E$) of the $Al_2O_3$–$SiO_2$ membrane to the four dyes is more powerful, as can be observed from the D–R curve, suggesting a stronger binding effect between the membrane and the dyes. Therefore, it is speculated that there are hydrogen bonds between the $Al_2O_3$–$SiO_2$ material surface and the dye structure.[34] The $TiO_2$/$Al_2O_3$–$SiO_2$ composite membrane exhibited high and stable water permeability to both anionic and non-ionic dyes and remarkable resistance to fouling. It is clear that there is competitive potential for water treatment with the composite membranes made in this work.

As shown in Table 4, we compare our work with other reported studies. The $TiO_2$/$Al_2O_3$–$SiO_2$ composite membrane exhibits excellent water permeability for dyes and maintains a high rejection rate for organic dyes. It demonstrates that the composite membrane prepared in this work has competitive potential in water treatment.

## 4. Conclusions

This work effectively prepared $TiO_2$/$Al_2O_3$–$SiO_2$ composite membranes using the sol–gel method to remove various ionic forms of organic dyes from water. Various analyses, such as $N_2$ adsorption–desorption, FTIR, XRD and SEM, were used to evaluate the fabricated composite membranes. FTIR analysis confirmed the presence of anionic hydroxyl groups in the membrane structure, facilitating interactions with the cationic dyes. Filtration experiments revealed that the average pore size of the $TiO_2$/$Al_2O_3$–$SiO_2$ membrane material increased with $n_{Ti}$, leading to a rise in membrane flux and a drop-in rejection rate. Considering the combined rejection rate and flux, the optimal filtration performance of the membrane appeared at $n_{Ti} = 0.15$. The CFSD model analysis of the experimental data suggests that the $TiO_2$/$Al_2O_3$–$SiO_2$ membrane is more conducive to dye molecule transport, which reduces the risk of solute accumulation and clogging on the membrane surface to some extent, and the separation efficiency of the membrane is relatively high.

The antifouling experiment revealed that the anionic dye RB-KNB is less likely to cause membrane fouling on the material, decreases membrane flux slightly, and has a high flux recovery rate. The FRR and IFR values of the $TiO_2/Al_2O_3$–$SiO_2$ membrane increased by 17.4% and decreased by 69.1%, respectively, after 6 cycles of filtering the RB-KNB dye, compared to the original membrane. The modified membrane maintains its separation stability for 20 h. The incorporation of $TiO_2$ improves the antifouling capabilities of the $Al_2O_3$–$SiO_2$ composite membrane, making this study extremely promising in the field of green and sustainable environmental governance. Future research could focus on expanding the applicability of membranes to pollutants, conducting simultaneous antibacterial performance testing, and improving their reusability by optimizing regeneration methods.

## Data availability

All relevant data are included within the paper. All data supporting the findings of this study are available within the paper and its ESI.†

## Author contributions

Qi Deng: conceptualization, methodology, formal, and writing. Jing Yang: funding acquisition and review & editing. Yuzhi Ai: project administration.

## Conflicts of interest

The authors declare that they have no known competing financial interests or personal relationships that could have appeared to influence the work reported in this paper.

## Acknowledgements

This work was supported by the Key Research and Development Projects of Shaanxi Province, China [2024GX-YBXM-491], the Nature Science Basic Research Plan in Shaanxi Province, China [2024JC-YBMS-361] and the Xi'an Municipal Science and Technology Project, China [23GXFW0023].

## References

1 R. J. Ganaie, S. Rafiq and A. Sharma, *IOP Conf. Ser. Earth Environ. Sci.*, 2023, **1110**, 012040.
2 A. N. M. A. Haque, R. Remadevi, X. Wang and M. Naebe, *Mater. Today: Proc.*, 2020, **31**, S221–S226.
3 A. M. A. Haque, N. Sultana, A. M. Sayem and S. A. Smriti, *Sustainability*, 2022, **14**, 11098.
4 J. W. Yoon, M. H. Baek, J. S. Hong, C. Y. Lee and J. K. Suh, *Korean J. Chem. Eng.*, 2012, **29**, 1722–1729.
5 A. K. Fard, G. McKay, A. Buekenhoudt, H. Al Sulaiti, F. Motmans, M. Khraisheh and M. Atieh, *Materials*, 2018, **11**, 74.
6 H. T. Thu, L. T. Dat and V. A. Tuan, *Vietnam J. Chem.*, 2019, **57**, 175–181.
7 C. Soma, M. Rumeau and C. Sergent, *Proc. 1st Intl. Conf. Membranes*, Montpellier, 1989, pp. 523–526.
8 S. Banerjee, D. D. Dionysiou and S. C. Pillai, *Appl. Catal., B*, 2015, **176–177**, 396–428.
9 Z. Zeng, X. Xiao, Z. Gui and L. Li, *Mater. Lett.*, 1998, **35**, 67–71.
10 M. L. Sun, T. B. Zhao, Z. F. Li, Z. F. Ma, J. Wang and F. Y. Li, *Ceram. Int.*, 2016, **42**, 15926–15932.
11 X. Xu, Y. Zhang, J. Wu and Z. Bai, *J. Wuhan Univ. Technol., Mater. Sci. Ed.*, 2003, **18**, 15–19.
12 J. Liu, Y. Li, B. Yin, S. Li and P. Chen, *Int. J. Appl. Ceram. Technol.*, 2022, **20**, 371–379.
13 Z. V. P. Murthy and S. K. Gupta, *Sep. Sci. Technol.*, 1996, **31**, 77–94.
14 J. Babu and Z. V. P. Murthy, *Sep. Purif. Technol.*, 2017, **183**, 66–72.
15 L. Shamaei, P. Karami, B. Khorshidi, R. Farnood and M. Sadrzadeh, *ACS Sustainable Chem. Eng.*, 2021, **9**, 15768–15779.
16 Q. M. Ahkam, E. U. Khan, J. Iqbal, A. Murtaza and M. T. Khan, *Phys. B Condens. Matter.*, 2019, **572**, 161–167.
17 J.-S. Jeng, L.-L. Yang and J. Chen, *Thin Solid Films*, 2017, **640**, 20–26.
18 R. Dalmis, N. F. A. Azem, I. Birlik and E. Çelik, *Appl. Surf. Sci.*, 2019, **475**, 94–101.
19 A. Adamczyk and E. Długoń, *Spectrochim. Acta, Part A*, 2012, **89**, 11–17.
20 J. Yang, Z. Xu, R. Mu, Y. Zhao, B. Li and H. Hou, *Integr. Ferroelectr.*, 2020, **207**, 220–230.
21 U. Anggarini, L. Yu, H. Nagasawa, M. Kanezashi and T. Tsuru, *Mater. Chem. Front.*, 2021, **5**, 3029–3042.
22 M. Sadeghi, G. Khanbabaei, A. H. S. Dehaghani, M. Sadeghi, M. A. Aravand, M. Akbarzade and S. Khatti, *J. Membr. Sci.*, 2008, **322**, 423–428.
23 L. Han, J. Ma, H. Lin, C. Chen, J. Teng, B. Li, D. Zhao, Y. Xu, W. Yu and L. Shen, *Chem. Eng. J.*, 2023, **470**, 144311.
24 J. Yang and Q. Liang, *Ferroelectrics*, 2019, **547**, 10–20.
25 M. E. Mahmoud, M. F. Amira, S. M. Seleim and A. K. Mohamed, *J. Chem. Eng. Data*, 2017, **62**, 839–850.
26 D. Cheng, J. Chen, J. Wang and X. Liu, *Heliyon*, 2023, **9**, e15979.
27 Y. Shi, X. Chen, Q. Wu, H. Zhen, S. Wang, H. Dong, J. Wang and Y. Li, *J. Environ. Chem. Eng.*, 2023, **11**, 110389.
28 S. S. Madaeni, S. Zinadini and V. Vatanpour, *J. Membr. Sci.*, 2011, **380**, 155–162.
29 S. S. Madaeni and N. Ghaemi, *J. Membr. Sci.*, 2007, **303**, 221–233.
30 X. Zhang, Z. Wang, M. Chen, M. Liu and Z. Wu, *J. Membr. Sci.*, 2016, **520**, 66–75.
31 J. Hou, Y. Chen, W. Shi, C. Bao and X. Hu, *Appl. Surf. Sci.*, 2020, **505**, 144145.
32 C. Wang, W. Zhang, C. Zhang, H. Xu, L. Liu and C. Zhang, *J. Membr. Sci.*, 2022, **663**, 121061.
33 L. Xiao, L. Chen, H. Xu, Z. Huang, Z. Wang, F. Liu, W. Wang and Q. Du, *RSC Adv.*, 2025, **15**, 9141–9152.
34 S. E. Gavabari, A. Goudarzi, M. Shahrousvand and A. Asfaram, *Sep. Purif. Technol.*, 2024, **330**, 125285.

35 Y. Wang, C. Bao, D. Li, J. Chen, X. Xu, S. Wen, Z. Guan, Q. Zhang, Y. Ding, Y. Xin and Y. Zou, *J. Membr. Sci.*, 2022, **661**, 120925.
36 F. Dai, G. Qian, Z. Ke, K. Xu, M. Wang, D. Li, Z. Deng, Y. Yu and C. Chen, *Sep. Purif. Technol.*, 2024, **345**, 127403.
37 A. Essate, D. El Machtani Idrissi, B. Achiou, S. Adlane, M. Breida, S. Curcio, S. Chakraborty, S. A. Younssi and M. Ouammou, *Colloids Surf., A*, 2024, **703**, 135162.
38 N. Prabhakar, A. M. Isloor, M. Padaki and A. F. Ismail, *Chem. Eng. J.*, 2024, **498**, 155270.
39 V. R. Pereira, A. M. Isloor, A. K. Zulhairun, M. N. Subramaniam, W. J. Lau and A. F. Ismail, *RSC Adv.*, 2016, **6**, 99764–99773.
40 I. M. Kolangare, A. M. Isloor, Z. A. Karim, A. Kulal, A. F. Ismail, Inamuddin and A. M. Asiri, *Environ. Chem. Lett.*, 2019, **17**, 581–587.
41 V. Vatanpour, S. Soylu, D. Osman, G. Tuncay, A. Mobaraki, Z. Marjani, A. Z. Halimehjani and I. Koyuncu, *J. Environ. Chem. Eng.*, 2024, **12**, 113308.
42 A. A. Neto, E. F. D. Januário, R. Bergamasco and A. M. S. Vieira, *Environ. Nanotechnol. Monit. Manag.*, 2024, **22**, 100954.
43 W. Y. Ye, J. Y. Lin, R. Borreg, D. Chen, A. Sotto, P. Luis, M. H. Liu, S. F. Zhao, C. Y. Tang and B. Van der Bruggen, *Sep. Purif. Technol.*, 2018, **197**, 27–35.
44 Y. C. Liu, Z. X. Yu, Y. X. Peng, L. Y. Shao, X. H. Li and H. J. Zeng, *Chem. Phys. Lett.*, 2020, **749**, 137424.
45 W. D. Ding, H. W. Zhuo, M. T. Bao, Y. M. Li and J. R. Lu, *Chem. Eng. J.*, 2017, **330**, 337–344.